Title
Developing a diagnostic for energetic laser-Compton produced photon beams

Authors
Quiter, BJ
Zhang, Y
Barton, PJ
et al.

Publication Date
2018-09-01

DOI
10.1016/j.nima.2018.06.031

Peer reviewed

Nuclear Inst. and Methods in Physics Research, A 903 (2018) 56–69

Contents lists available at ScienceDirect

Nuclear Inst. and Methods in Physics Research, A

journal homepage: www.elsevier.com/locate/nima

Developing a diagnostic for energetic laser-Compton produced photon beams

B.J. Quiter [a,*], Y. Zhang [a,b], P.J. Barton [a], C.G.R. Geddes [a], M. Garcia-Sciveres [a], M. Janecek [a,c], K. Vetter [a,b]

[a] Lawrence Berkeley National Laboratory, Berkeley, CA, USA
[b] Department of Nuclear Engineering, University of California, Berkeley, CA, USA
[c] Now with Hamamatsu Corporation, USA

ARTICLE INFO

Keywords:
Particle tracking detectors
Pixelated detectors
Laser-Thomson scattering
Laser–plasma accelerators
Compton spectrometer
MeV gamma-ray imaging
Charge-Coupled Device (CCD)

ABSTRACT

This paper describes the design and simulation of a radiation detector system for diagnostic measurements of photon beams produced by Thomson or Compton Scattering. The photon beam is Compton scattered in a thin passive converter, and the resulting electrons are analyzed using a charge-coupled device-based tracker and classification algorithms. The flux of the scattered electrons is much lower than that of the photon beam and is additionally dispersed. This dispersal enables measurements while avoiding pileup, which is important in order to provide diagnostic information from intense 'shot' based pulsed systems, such as those being built to leverage laser wakefield accelerators. Simulations indicate that the designed system is capable of resolving beam parameters from a single shot. The fidelity to which various beam parameters can be resolved is presented as are methods that could result in further improvement to diagnostic resolution.

1. Introduction

High-intensity, narrow energy-spread photon beam sources are being developed for use in applications such as nuclear security [1], non-proliferation [2] and safeguards [3,4] as well as for explosives detection [5], molecular structure studies [6], and for experimentally testing nuclear and quantum electrodynamic theories [7,8].

Very narrow energy-spread photon beams may be produced by nuclear transitions, but obtainable energies are restricted by nuclear structure, while intensity, portability, and sustainability are major issues. Therefore, laser-Thomson scatter sources, also known as laser-Compton sources (LCS), where highly relativistic electron beams (300–700 MeV) undergo scattering with ~1 μm laser light, are important candidates to produce MeV-class photon beams. Their beams also have milliradian (mrad) divergence which mitigates scattering contributions to image contrast degradation and allows high spatial resolution and/or measurement of targets at a distance. Source energy spread is most critical for nuclear security, non-proliferation, and safeguards near 2 MeV, where Nuclear Resonance Fluorescence (NRF) measurements benefit from low (<few%) energy spread [2]. Energies up to approximately 10 MeV are also of interest for photo fission and radiography applications, albeit with looser tolerances on energy spread. The High Intensity Gamma Source (HIGS) at Triangle Universities Nuclear Laboratory is an example of such a source [9]. At HIGS, the electron beam is kept in a storage ring and the laser light is produced by inducing Free Electron Laser (FEL) radiation from the electron beam. As a result, the beam is produced with a high repetition rate (~MHz), has relatively low per-pulse intensity, and requires a footprint of hundreds of square meters. Conversely, LCS sources that use intense lasers and compact laser–plasma accelerators (LPAs) are being developed [10,11]. LPAs can achieve the required electron energies in cm-scale plasmas. Such sources have the potential to deliver a photon beam with similar energy spread and with high flux in a small footprint. However, instead of a MHz repetition rate beam, they are anticipated to deliver pulses of approximately 10^8 photons per shot at repetition rates up to a few kHz. Proof of principle experiments typically operate at up to few Hz rates. Future sources based on radio frequency linear accelerators (linacs) are also anticipated to deliver high flux per shot [12]. To develop such next-generation sources, diagnostic systems capable of efficiently characterizing the pulsed MeV-photon beams are needed.

Diagnostics for HIGS-type beams have been developed, either based on integrating a scintillator signal (see [13]), by continuous indirect measurement of MHz beams (see [9,14]). However, these diagnostics cannot provide sufficient per-shot diagnostic information to facilitate

* Corresponding author.
E-mail address: bjquiter@lbl.gov (B.J. Quiter).

https://doi.org/10.1016/j.nima.2018.06.031
Received 6 April 2018; Received in revised form 8 June 2018; Accepted 11 June 2018
Available online 25 June 2018
0168-9002/

development of beams operating at the few Hz rates of near-term LPA-based source development experiments. Single shot information is also desired to characterize source fluctuation. Single shot measurement of keV energy linac or LPA-driven LCS beams [15–18] have been accomplished using CCDs designed to fully absorb X-ray energy photons. However, these methods do not work well at MeV energies due to spatial extent of the photon-induced charge being comparable to the beam diameter at laboratory distances. Filter based techniques have also been used but have low resolution [18–22]. Compton scattering to disperse the flux of MeV photon beams is a promising approach [14,23–27], but so far has resulted in energy resolution >10%, which is not sufficient for high-quality photon sources. Compton spectrometers that measure energies of individual Compton electrons have also been demonstrated, but the lack of spatial resolution of such methods and challenges related to applying such a system to an LCS source detract from the appeal of implementing such a method [28,29]. More recently, an array of scintillating CsI(Tl) detectors were placed directly in a beam of 100's of MeV γ rays produced via LCS and the relative light output of the series of detectors along the beam trajectory was used to constrain characteristics the gamma-ray beams and LCS process [30].

In this paper a single-shot diagnostic system capable of high resolution measurement of a pulsed beam of photons with centroid energies near 2 MeV – the most demanding range for application energy spread – will be discussed. Aspects of this work have been proposed previously [31,32]. Source beam photons pass through a thin target, where they produce secondary electrons via Compton scattering. These scattered secondary electrons can be measured by a tracking detector placed outside the photon beam. Simulations were principally conducted using the GEANT4 Monte Carlo simulation toolkit [33]. The simulation of expected photon beam profiles as input to the diagnostic simulations were separately conducted using the CCSC code [13], which numerically integrates differential cross sections for Compton scatter to produce likely photon beam profiles. The modeling and the beam selection criteria indicate that relevant beams with electron energy spreads of 4.5%, 12% and 24% FWHM can be distinguished with an average true-positive probability of 80% and that beams with angular spreads between 0.19, 0.43, 0.84 and 1.75 mrad can be distinguished with a similar average true-positive probability. The modeling also indicates that energy resolution and spatial resolution of the diagnostic system are strong functions of the position on the CCD at which each Compton electron is measured.

This paper is organized as follows. The photon beam characteristics that are to be distinguished by the diagnostic system are described in Section 2. Section 3 uses GEANT4 simulations to directly assess passive converter designs where photons undergo Compton (or incoherent) scatter to produce electrons that will be measured in the electron tracking system. Section 4 uses GEANT4 (and GATE) to assess designs of that system by simulating electrons incident upon a set of potential tracking system designs. Upon having identified a tracking system, Section 5 uses more detailed GEANT4 calculations to estimate the response of the electron tracker system to a mono-energetic and mono-directional beam of photons in both determination of the electron properties and with respect to reconstructing the energy and interaction position of the original photon. Finally, in Section 6, the entire diagnostic system is modeled in GEANT4 for a series of beams and estimates of the system performance are derived based on a simple means of discretizing the observed signal and comparing it with various expectations.

2. Beam descriptions

The phenomenology of laser-Compton scatter photon beams has been described in detail elsewhere (e.g. [9,34,35]), including the anticipated characteristics of LPA-generated photon sources [10,36]. For a single relativistic electron (i.e., $v_e \approx c$) with energy, $E_e^B = \gamma m_e c^2$, (the superscript ^{B} refers to beam electrons and here γ is the Lorentz factor) in a uniform field of laser light with energy E_L, the produced energetic photons have energies given by,

$$E_\gamma = \frac{2\gamma^2(1-\cos\phi)E_L}{1+a_0^2/2+\gamma^2\theta^2} \quad (1)$$

where ϕ is the angle between the incident laser light and the electron beam, typically chosen to be 180° for the highest energy up-shift and to minimize walk of the electron and photon beams, and a_o is the dimensionless laser strength parameter. The angle between the scattered energetic photons and the relativistic electrons is denoted as θ. It can be seen that the highest energies are emitted along the electron axis, falling off to half energy near $\gamma\theta = 1$ radian (rad). The emission intensity also falls off over this characteristic angle [10]. Collimation to $\gamma\theta < 1$ rad is therefore required to obtain narrow energy spread.

When a beam of electrons distributed normally in energy with mean energy $\bar{E}_e^B$, and root-mean-square energy spread, $\sigma_{E_e^B}$, and with angular spread, $d\theta$, interacts with a laser beam, the resulting LCS beam energy and angular distribution may be determined by integrating the response. The alignment of the electron beam, relative to the nominal direction, is typically anti-parallel, i.e., $\phi = \pi$. Here, the assumption is made that the laser beam is uniform over a dimension larger than that of the electron beam, and that there is no misalignment. Typical laser beam diameters are $\gtrsim$ 10μm while the nominal electron beam diameter is 0.1–1 μm. Lastly, $a_0 = 0.85 \times 10^{-9}\lambda\ [\mu m] \times (I\ [W/cm^2])^{1/2}$ is small enough to be ignored herein. For treatment of these effects see, e.g. [10] and others.

Laser-Compton Scatter sources currently operating and under development typically have energy spread at the few to 10% level, and there is development in progress to push energy spread down to or below the 1% level. Similarly, LPA-driven sources presently have energy spreads at or above the 10% level but with development, energy spreads similar to conventional systems are anticipated since electron energy spreads down to the 1% FWHM level have been demonstrated and there are indications of narrower energy spread (see [37] for a review on the subject). These levels motivate diagnostic requirements at the 10% energy spread level in the near term and below the 1% level in the long term, respectively. A particular need for LPA based systems is that the electron beam divergence from 0.5 GeV-class LPAs is on the level of 1 mrad ($\gamma d\theta \sim 1$) because of the strong focusing inside the plasma wave. As a result, the electron beam angular contribution is typically the dominant contributor to photon energy spreads for scattering in the plasma. Hence diagnostics capable of distinguishing photon beam spectral features resulting from electron energy spread versus angular spread are important. In the long term reduction of beam divergence, by either improved LPA control or by recollimating the electron beam, will be the path to achieve energy spreads at or below the 1% level limited by the electron energy spread. In typical photon source experiments, the electron beam energy and energy spread are adjustable and can be measured to 1% using a magnetic spectrometer [38]. The electron beam divergence is also measured in the undisposed plane of the magnetic spectrometer. The value of E_L will be well-known due to the type of laser that will be used. For example using an 800 nm Ti:sapphire laser and $E_e^B = 272$ MeV produces $E_\gamma = 1.73$ MeV with $\theta = 0$ and $\phi = \pi$ and for 1 cm^2 PW lasers ($a_0 = 0.02$).

The goal of the MeV photon detector is then to demonstrate the capacity to achieve in a single source shot both energy resolution and ability to distinguish between effects from electron energy spread and divergence. For near-term experiments, the capability to distinguish between beams that differ by 5% in energy spread and/or by a fraction of a mrad in divergence would be a useful step and would support near-term photon source experiments at the 10% level of energy spread appropriate to radiography or photo fission applications [2]. In the long term, resolution of electron energy spread at or below the 1% level and of electron angular spreads at the 0.1 mrad level would enable development of photon sources at and below the percent level in energy spread relevant to Nuclear Resonance Fluorescence (NRF) applications [2].

Figs. 1 and 2 compare a nominal calculated γ-ray beam profile to different beam profiles produced by characteristic source variations

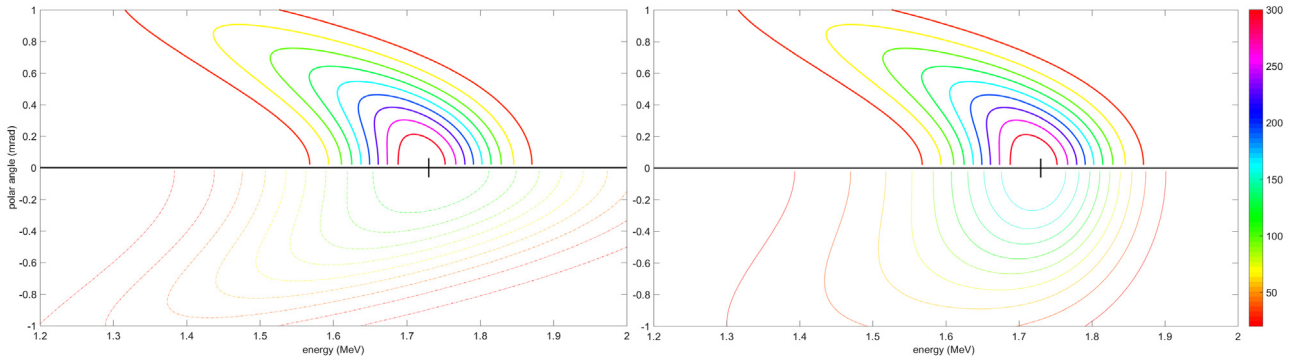

Fig. 1. Left: Intensity contours of the nominal beam ($d\theta = 0.19$ mrad, $\delta E_e^B/E_e^B = 4.5\%$) (bold) transmitted through a 1-cm diameter collimator 5 m from collision point along the laser polarization axis compared with a wider angular spread ($d\theta = 0.4$ mrad) beam shown as normal-weight contour lines and flipped vertically; and **Right:** with a larger energy spread ($\Delta E_e^B/E_e^B = 10\%$) beam shown as the dot-dashed contour lines and flipped vertically. All three intensity profiles are normalized by the number of photons through the collimator and the color-scale units are 1/eV/str. The maximum ordinate value corresponds to the edge of the simulated collimator and the color-scale was selected to highlight intensity changes in the lower intensity portions of the surfaces. In this scale the red contour indicating low intensities corresponds energies and/or angles furthest from the beam centroids, which are indicated as the thick black lines. (For interpretation of the references to color in this figure legend, the reader is referred to the web version of this article.)

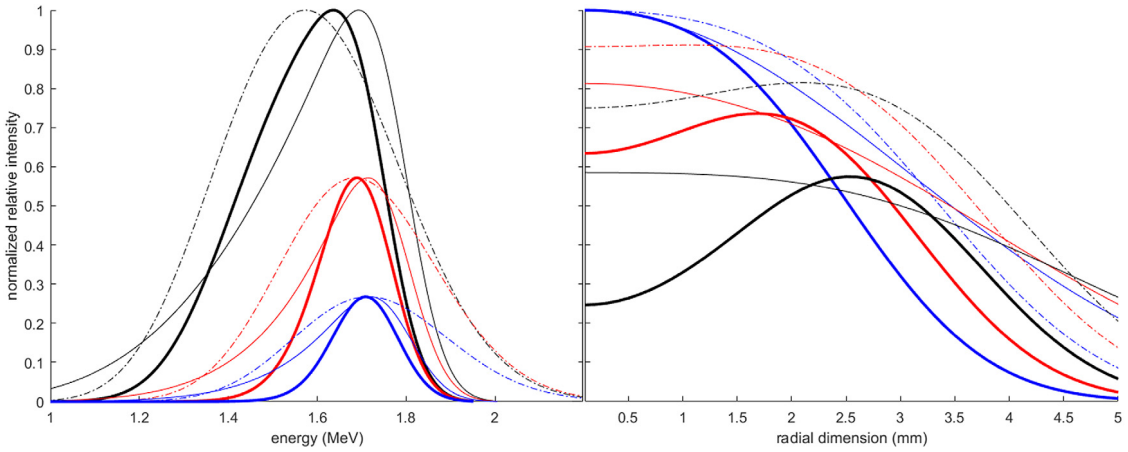

Fig. 2. Left: Comparing energy distributions of example beams by integrating normalized beam profiles from the center of the beam to different maximum radii. The blue curves correspond to integration up to a diameter of 3 mm, the red to 5 mm, and the black to the entire 1 cm-diameter beam. The curves are normalized as follows: the nominal beam is normalized relative to the entire beam profile, whereas the two other beams are normalized relative to the peak intensity of the nominal beam at each radial dimension (this was done to facilitate comparisons). **Right:** Comparing radial profiles of the example beams at 1.7 (blue), 1.65 (red), and 1.6 (black) MeV. All beams are normalized relative to the peak intensity at 1.73 MeV. For both images, the nominal beam is indicated as the bold curves, the larger $\sigma_{\delta E_e^B}$ beam is shown as the dot–dash curves, and the larger $d\theta$ beam is the solid curves. (For interpretation of the references to color in this figure legend, the reader is referred to the web version of this article.)

that the diagnostic system should address. The nominal photon beam is produced by an electron beam of $E_e^B = 272$ MeV ($\gamma = 533$), $\sigma_{E_e^B} = 4.6$ MeV ($\Delta E_e^B/E_e^B = 4.5\%$) and $d\theta = 0.19$ mrad interacting with a Ti:sapphire laser. The nominal spectrum is always shown as the heavy solid lines. Each spectrum is plotted over $\gamma\theta = 0$–1.0 mrad, corresponding to a 1 cm-diameter collimator diameter 5 m from the LCS interaction point, which is representative of a realistic laboratory setup.

Two spectra illustrating changes in electron beam energy spread or divergence conditions that should be distinguishable via the photon signal are compared to the nominal spectrum. The first compared beam profile differed from the nominal beam in that angular spread is increased, $d\theta = 0.4$ mrad resulting in a beam whose energy distribution is less dependent upon the radial position within the beam. Note that the electron beam energy was also increased by 1.4% for this beam to compensate for the slight reduction in centroid energies that result when the broader electron angular spread beam produces up-scattered photons. This increased angular spread beam is indicated with the thinner solid lines in the figures. The second compared beam profile differed from the nominal beam in that the electron beam energy distribution was $\Delta E_e^B/E_e^B = 10\%$, resulting in a broader and less intense energy distribution at all energies. Fig. 1 shows contour representations of the normalized beam intensity as a function of angle, θ and up-shifted photon energy, E_γ, along the laser polarization axis comparing the nominal beam to the larger $d\theta$ beam on the left and to the larger $\sigma_{E_e^B}$ beam on the right. Along the radial dimension perpendicular to the polarization axis, the beam intensities decrease less rapidly with increasing angle, but the relationship between energy and polar angle remains.

In Fig. 2, energy profiles and radial profiles of the example beams are shown using the same drawing conventions (bold for the nominal beam, dot–dash for the higher energy-spread beam and thinner solid line for the broader angular spread beam). In the left figure, radially-integrated energy distributions of the three beams shown in Fig. 1 are shown within diameters of 3, 5 and 10 mm as the blue, red and black curves, respectively. Each spectrum is normalized to the total number of γ rays transmitted through the 1 cm-diameter collimator. While spectral differences do exist, one concern is whether a difference generated by an electron beam shifted in centroid energy could be distinguished from one due to differing angular spread. While the energy-integrated radial profiles of different beams can also look very similar (changes in

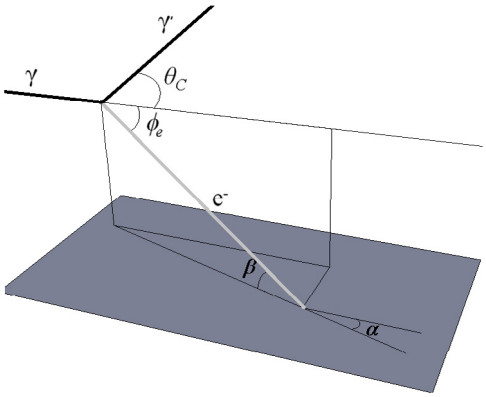

Fig. 3. Compton scattering schematic, particle trajectories are shown as thick lines (photons are black and the Compton electron is light). Angles relative to a detector plane (dark gray), α and β are also specified via orthographic projection.

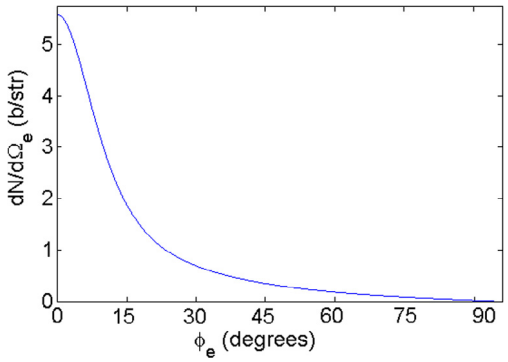

Fig. 4. Compton differential cross section for incoherent scatter as a function of electron recoil angle, ϕ_e.

ΔE_e^B have nearly no impact on radial profile), the right figure indicates E_γ = 1.7, 1.65, and 1.6 MeV radial profiles in blue, red and black, respectively. The nominal beam is more intense in the center than either the broader energy-spread beam or the broader angular spread beam and drops more in energy at larger radii than does the larger angular spread beam. This indicates that a diagnostic that can measure both energy and radial profiles will likely be the most effective.

The goal of the design study described in the following is to demonstrate the capacity for a measurement system to distinguish – in a single shot – between the nominal beam and beams that differ in either $\sigma_{E_e^B}$ or $d\theta$, or both. Because of similarities between radially-integrated energy profiles and energy-integrated radial profiles, it was decided that the diagnostic system should be capable of resolving in both energy and angular space simultaneously.

3. Mega electron volt photon detection

Whereas the LCS beam diagnostic described in Ref. [17] was able to use a pixelated CCD positioned within the beam to measure the energy and position of incident photons, the physics associated with detecting 12 keV photons differs significantly from that associated with measuring multi-MeV photons. In the former case, photoelectric absorption – wherein the photon energy is transferred to ionizing an atomic electron – is the primary photon interaction mechanism. Resulting photo-electrons have a range of 1.5–2 μm in Silicon and therefore are typically confined to a single CCD pixel. In the case of MeV photons, incoherent scatter and pair production dominate, producing recoil electrons with much longer ranges. This limits use of finely pixelated detectors. In the following, we have selected to use low-atomic number materials to minimize pair production and examine imaging the incoherent scatter products as a beam diagnostic. Conversely, either at higher energies or by selecting a high-Z converter material, one could select to image the electron–positron pairs, as is described in Ref. [27].

Incoherent scatter of 1.7 MeV photons is well-approximated by the Compton formalism, wherein a Compton electron recoils with energy,

$$E_e = \frac{2E_\gamma \alpha_e \cos^2\phi_e}{\alpha_e^2 \sin^2\phi_e + 2\alpha_e + 1} \tag{2}$$

where $\alpha_e = E_\gamma / m_e c^2$, and the Compton-scattered γ ray retains energy according to,

$$E_\gamma = \frac{m_e c^2}{\xi \cos\phi_e - 1}. \tag{3}$$

where $\xi = \sqrt{1 + \frac{2m_e c^2}{E_e}}$.

A schematic describing this interaction is shown in Fig. 3. The cross section for electron scatter as a function of ϕ_e is shown in Fig. 4. Incoherent scatter tends to produce energetic and forward-directed electrons. However, taking solid angle into account yields a mean emission angle of ϕ_e = 30° and the most probable electron emission angle is ϕ_e = 10°. These angles correspond to recoil electron energies of 0.8 and 1.4 MeV, respectively. The relationship between ϕ_e and E_e is shown in red in Fig. 5.

Continuous slowing down approximation ranges for 0.5–1.5 MeV electrons in silicon range from 1 to 4 mm [39] and scale closely with electron density in the material. Given the tortuous trajectory electrons typically undergo as they slow, only a handful of electrons could be individually resolved by placing a semiconductor-based radiation detector system within the beam. With this in mind, three potential beam diagnostic methods appear plausible; to use a gaseous detector system — wherein the electron track density decreases proportionally to the detector material electron density; or to use (one or more) thin layers of passive scattering material to produce recoiling Compton electrons that are measured outside of the beam envelope. Other work has described use of a magnetic spectrometer to analyze the scattered electrons [25,27–29]. Here we address the scattering method using a CCD based tracker. The trajectory and energy of the recoiling electron can then be reconstructed to determine the interaction location and energy of the beam γ ray via Eq. (2).

The passive γ-ray scatterer (referred to herein as the converter) material was selected to be nitrocellulose (ρ = 1.6 g/cm^3) although any thin film comprised of low-Z constituents could be used. For nitrocellulose, the number of Compton electrons expected to be produced per 1.7-MeV incident beam photon, per μm is 7.9×10^{-6}[40]. Thicker layers of passive material generate more scattered electrons, but also result in more deflection of recoil electrons within the passive material. GEANT4 simulations [33] were conducted to examine this phenomenon and to more precisely simulate the incoherent scatter and Doppler-broadening processes in the converter. In these simulations, nitrocellulose slabs of varying thicknesses were irradiated by mono-directional 1.7 MeV photons and the directions and energies of each electron were determined both upon production and leaving the nitrocellulose. Fig. 5 shows the results from simulations of the 10 μm-thick nitrocellulose with 5×10^6 incident photons. The produced electron energies and angles (solid blue dots) and those of electrons leaving the nitrocellulose (green open circles) are plotted, with solid blue lines connecting each pair of points due to the same electron. Also shown in red is the expected energy–angle relationship given by Eq. (2). The spread of the initial electron data points around the Compton kinematics line results from Doppler broadening that occurs when photons interact with bound electrons. Fig. 5 indicates that after leaving the passive converter, the low energy electrons are appreciably less likely to accurately indicate the initial value of ϕ_e, but those measured with more than approximately 500 keV

Table 1
For 10^8 incident photons, the number of Compton events, N_C, that will occur within a passive nitrocellulose converter of thickness, x_{nitro}, the number of Compton electron that will escape the down-beam side of the converter, N_{esc}, the number of electrons that will also have retained their trajectory and energy such that they could be reconstructed to within 20% of their initial energy, $N(\Delta E_\gamma^c < 20\%)$ while also having scattered at an angle, $\phi_e > 10°$, which roughly represents a large enough scattering angle to intercept a out-of-beam tracker. Of the $N(\Delta E_\gamma^c < 20\%)$ photons, $f_{2\%}$ are the fraction that could be reconstructed to within 2% of their initial energy. The last two columns show the number and corresponding fraction of Compton events that would additionally exceed a 500 keV energy threshold.

x_{nitro}	# electrons/10^3		$\phi_e > 10°$		$E_e > 500$ keV, $\phi_e > 10°$	
(μm)	N_C	N_{esc}	$N(\Delta E_\gamma^c < 20\%)$	$f_{2\%}$	$N(\Delta E_\gamma^c < 20\%)$	$f_{2\%}$
7.5	6.0 ± 0.4	5.8 ± 0.3	4.7 ± 0.3	0.84 ± 0.02	3.3 ± 0.3	0.97 ± 0.01
10	8.1 ± 0.3	7.9 ± 0.3	6.2 ± 0.3	0.84 ± 0.02	4.4 ± 0.2	0.98 ± 0.01
15	12.2 ± 0.5	11.5 ± 0.5	9.0 ± 0.4	0.82 ± 0.02	6.6 ± 0.4	0.97 ± 0.01
20	16.1 ± 0.6	15.2 ± 0.6	11.7 ± 0.5	0.80 ± 0.02	8.4 ± 0.4	0.95 ± 0.01
25	20.5 ± 0.6	19.2 ± 0.6	15.4 ± 0.6	0.81 ± 0.01	11.7 ± 0.5	0.94 ± 0.01
30	25.7 ± 0.7	24.2 ± 0.7	19.2 ± 0.6	0.76 ± 0.01	14.3 ± 0.5	0.92 ± 0.01
40	32.8 ± 0.8	30.6 ± 0.8	24.3 ± 0.7	0.76 ± 0.01	18.3 ± 0.6	0.91 ± 0.01

generally retain a good amount of energy and angle information. For such electrons, Eq. (3) could be used to provide an estimate of the initial photon energy and position upon scattering in the nitrocellulose layer. Uncertainties result from both energy/spatial resolutions in the electron sensor and energy/angle straggling within the converter. We address the latter here and the former in Section 5.

Deflections of electrons result in non-zero values of $\Delta\phi_e$, and energy loss mechanisms result in $\Delta E_e < 0$. Although this is addressed later through modeling, for now the approximation is made that energy loss and angular deviations are uncorrelated. The error in energy determination due to effects in the converter, ΔE_γ^c, is then given by,

$$\Delta E_\gamma^c = \sqrt{\left(\frac{\delta E_\gamma}{\delta \phi_e}\Delta\phi_e\right)^2 + \left(\frac{\delta E_\gamma}{\delta E_e}\Delta E_e\right)^2} \tag{4}$$

where $\Delta\phi_e$ is the difference between the angle ϕ_e of the emitted electron and upon creation, and ΔE_e is the energy lost by the electron as it leaves the converter.[1] Using Eq. (3), we have

$$\frac{\partial E_\gamma}{\partial E_e} = \frac{m_e^2 c^4 \cos\phi_e}{E_e^2 \xi(\xi\cos\phi_e - 1)^2} \tag{5}$$

and

$$\frac{\partial E_\gamma}{\partial \phi_e} = \frac{m_e c^2 \xi \sin\phi_e}{(\xi\cos\phi_e - 1)^2}. \tag{6}$$

For a range of simulated nitrocellulose converter thicknesses, x_{nitro}, the second and third columns of Table 1 indicate the number of Compton electrons created, N_C, and the number that escape the back end of the converter, N_{esc}, both in units of 10^3 electrons per 10^8 photons incident upon the converter (i.e. per anticipated photon source 'shot'). Given that any Compton electron tracker will be positioned outside of the beam envelope, we note how many of the escaping electrons have an emitted electron angle greater than 10°. We also assert (detailed below) that those electrons that have undergone sufficiently severe deflection or energy loss will be distinguishable as having done so, and therefore, we consider the case where the reconstructed γ-ray energy is accurate to within 20%. The number of electrons meeting these requirements is given in the fourth column of Table 1, $N(\Delta E_\gamma^c < 20\%)$ for $\phi_e > 10°$, and the fraction of those electrons that could be reconstructed to provide a γ-ray energy accurate to within 2% is given in the fifth column, $f_{2\%}$. Clearly, increased converter thickness results in fractionally fewer electrons that provide valuable information for γ-ray event reconstruction, but even for thin converters, more than 15% of the electrons could not be used by a perfect detector to reconstruct beam photon energies to within 2%. Instead, we consider those electrons that escape the converter with $\phi_e > 10°$ and that retain greater than 500 keV. In this case, the number of electrons that resulted are shown in the 6th column and the corresponding fraction that could be reconstructed with $\Delta E_\gamma < 2\%$ are shown in the final column. Without an estimate of the beam reconstruction performance, we cannot make firm conclusions, but it appears that applying an energy cut on the measured electrons is beneficial. A converter of thickness 10–30 μm is likely reasonable, and such a converter will produce 4400–14,000 potentially useful Compton electrons outside of the beam envelope after a shot of 10^8 photons. These general results were used as basis for detailed design simulations.

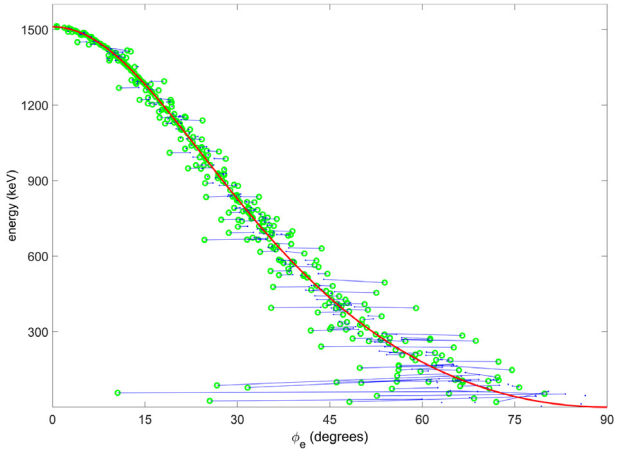

Fig. 5. Simulated recoil electron energies and angles upon excitation (blue dots) and emission from 10 μm nitrocellulose (green circles), compared to Compton Kinematics (red). Solid lines connect the initial electron parameters to those at emission. (For interpretation of the references to color in this figure legend, the reader is referred to the web version of this article.)

4. Electron imager design concepts

Having gained understanding of the effects of the passive scatterer, a second set of simulations were conducted wherein the limits on detector spatial resolution were investigated for potential placements of the electron tracking system. The four configurations shown in Fig. 6 were each simulated using two types of pixelated Si detectors. In each simulation, the beam consisted of a 1.7 MeV mono-energetic, mono-directional zero-radius (pencil) beam. The detectors were modeled as 19 mm × 19 mm Si pixelated devices and were either 50-μm thick with 10.5 μm pixel pitch or 15-μm thick with 2.5 μm pixel pitch, referred to as Detectors *A* and *B*, respectively. The 'Detector A' configuration is considered representative of scientific CCD-based technologies [41] wherein no interpolation between pixels is conducted. The 'Detector B' configuration roughly corresponds to the position resolution that

[1] Using GEANT4, the primary electrons are followed to make this estimate.

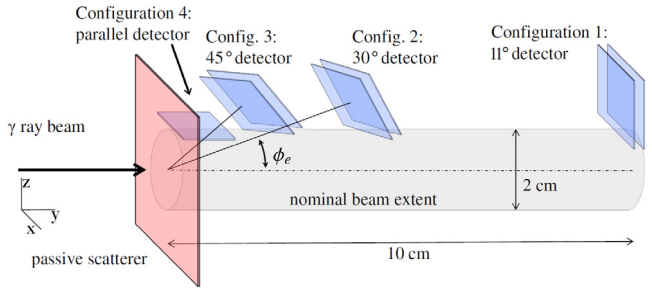

Fig. 6. Schematic representation of design concept configurations.

Table 2
Percentages of trajectories that reconstruct to within 10 mm of the actual position on the converter for models of two types of Si detectors (A and B) and for three configurations. See text and Fig. 6 for further details.

#	$r < 1$ cm (%)
1_A	11
2_A	44
3_A	53
4_A	94
1_B	48
2_B	86
3_B	93

could be achieved from interpolating diffused tracks within a monolithic active pixel sensor array (MAPS) [42] that are thinned behind the active area subsequent to production.

For each detector type and each configuration, two detectors were placed downstream of the converter in vacuum. The front detector was positioned such that the edge nearest to the beam centroid was 1 cm from the axis of the photon beam (in the direction the z-axis) and was positioned downstream (along the y-axis) of the converter at a distance such that the Si was centered at angles of 11°, 30°, and 45° relative to the beam axis centroid (referred to as Configurations 1–3, respectively). For each of these configurations a second detector (the back detector) was placed 5 mm behind and parallel to the front detector. Electron interaction positions were noted as the electrons left the converter and passed through the two detectors. The pixels at which the electrons entered the detectors were used to reconstruct each electron's trajectory by tracing a line through the center of these two pixels. The intercept location of this line at the converter plane was compared to the true position of electron emission. As a cursory means of estimating the resolution of each configuration, the fraction of event reconstructions that were within 1 cm of the true position are shown in Table 2.

Although Compton electrons with more energy (and smaller ϕ_e) lose less information as they leave the converter, the requirement that the detector system be outside the beam envelope results in larger stand-off distances when the detector angle is reduced. These increased distances result in worse position reconstructions for these configurations. Conversely, larger angles of ϕ_e result in more information loss within the converter. These conflicting trends and the results in Table 2 indicate that track reconstruction using parallel planar detectors oriented normal to a ray between the detector and the interaction point would produce poor performance unless the front detector is very thin and is capable of position resolution much better than 10 μm. While feasible, the utilization of such thin detectors is difficult compared to the thicker options. Instead, positioning the electron imaging system as close to the passive converter is ideal and Configuration 4 (as indicated in Fig. 6) also achieves excellent fidelity while accommodating thicker and therefore easier-to-handle detectors. In this configuration the detector is placed parallel to the beam trajectory and just adjacent to the beam profile. This minimizes the distance between the converter and the tracker while still subtending much of the solid angle that corresponds to smaller values of ϕ_e. This configuration also causes electrons to traverse multiple pixels within the detector, which facilitates electron trajectory determination. This configuration is examined in further detail in the following, although the diameter of the assumed collimator is reduced from 2 cm to 1 cm in light of the findings from this set of simulations.

5. Parallel tracker performance

The precision to which the beam photon interaction positions and energies can be reconstructed is limited by the ability to measure directions and energies of the produced secondary electrons. Section 3 summarized the loss of information due to the converter. In this section, the effects of the tracker were investigated by studying the behavior of electrons emitted from the converter as they interact within Si tracker material. This study was conducted using GEANT4 simulations with the Penelope physics package [43] using a 500 nm StepFunction parameter, rather than the default 100 μm. This parameter modification results in prioritizing simulation precision over speed and ensures that the effects of Coulombic forces are traced with better fidelity than the pixel dimensions. Because of material availability, the investigation focuses on a 650 μm-thick pixelated Si CCD, with 10.5 μm pixel pitch. Simulated CCDs additionally had face dimensions of 8.4 cm × 8.4 cm. This will be the reference CCD geometry hereafter.

Energies and positions of source beam photons that interact with the converter were individually reconstructed through analyses of the electron interactions within the tracker system. Positions at the converter are determined by tracing a ray back to the converter starting from the reconstructed position of incidence of the Compton electron upon the tracker. The reconstructed direction of the incident electron in the tracker was used to determine the orientation of the traced ray and hence to reconstruct the position from which the electron was emitted from a photon interaction in the converter. Photon energies were then reconstructed using Eq. (3), which determines the photon energy given the tracker-determined Compton electron direction and reconstructed electron energy.

Tracker performance is dependent upon the angle of incidence and the energy of the incident electron. Therefore, the effective angular and spatial resolution expected from the tracker depends on each electron's incident positions upon the tracker. The angular resolution of the tracker is studied by simulating electrons impinging upon slab of Si. For analysis, the direction of the Compton electron is decomposed into two angles, the in-tracker-plane angle, α, and the out-of-tracker-plane angle, β (indicated in Fig. 3). The quantities ϕ_e, α, and β are related by,

$$\cos\phi_e = \cos\alpha\cos\beta \tag{7}$$

The simulations were performed for β ranging from 10° to 40°. Electron energies are computed using $E_\gamma = 1.73$ MeV for each $\phi_e = \beta$. In post-processing, the effects of charge diffusion and pixelization were considered for a Si slab. The point of incidence of each source electron was randomized with respect to the pixel grid for each energy deposition, as was the angle in the plane, α. Diffusion of the liberated charge was simulated as described in Ref. [44]. The result of this post-processing is a two-dimensional electron track image for each simulated electron, as is anticipated from a pixelated Si detector. An example image is provided in Fig. 7. The electron track images are subsequently analyzed as described in detail below, producing an incident vector that may be compared with the true incident vector from the simulation. The reconstructed electron trajectory vector is described by the reconstructed vector angle in the plane, α_r, and the reconstructed vector angle relative to the plane, β_r. The differences between these values and the true simulated trajectories are determined to produce values of Δ_α and Δ_β. The method for reconstructing α_r and β_r was described elsewhere [44], but it is worth noting that the two angles are determined separately. Track reconstruction begins by first selecting contiguous pixels for which an energy depositions

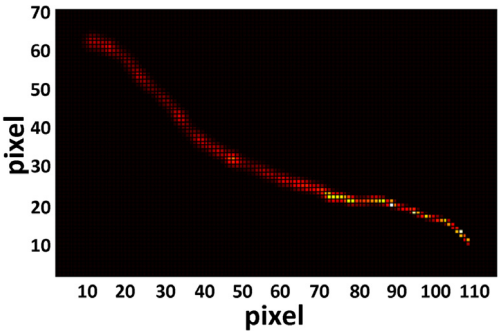

Fig. 7. An example simulated electron track from a 1.2 MeV electron incident upon the back plane of a 650 μm-thick Si CCD with 10.5 μm pitch pixels at 20° angle of incidence relative to the detector plane. The electron is incident in the top-left of the figure.

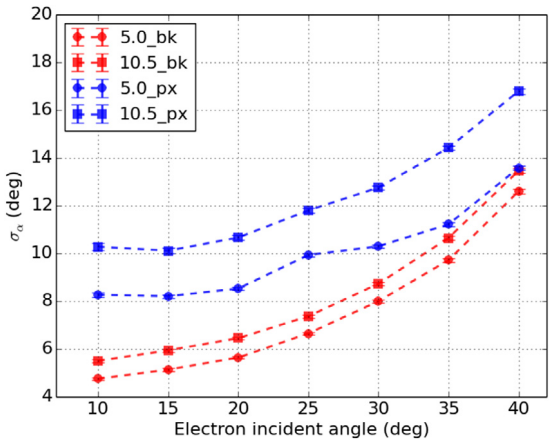

Fig. 8. Simulated angular resolution for determining the trajectory of an incident electron upon a 650 μm-thick slab of Si where the energy of the electron is given by Eq. (2) and the electron incident angle, $\beta = \phi_e$. The squares indicate 10.5 μm pixel pitch whereas the squares indicate 5 μm pixel pitch. Blue indicates pixel plane irradiation and red indicates irradiation on the non-readout side of the Si slab. (For interpretation of the references to color in this figure legend, the reader is referred to the web version of this article.)

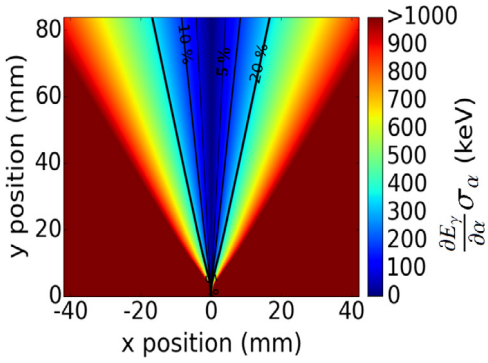

Fig. 9. Expected contribution to energy resolution due to α angular resolution for given electron incident position on the CCD.

greater than some threshold energy has occurred. Thereafter, the beginning of each track is identified. In sufficiently thick detectors (i.e., those with appreciably diffusion), the end of the track corresponding to the electron entrance can often be identified by that end with the least/most diffusion for irradiation upon the pixel-plane/back-plane of the CCD. Tracks that wrap around themselves are rejected from the reconstruction algorithm. Similarly, track ends that would reconstruct to α_r values >90° (i.e., pointing away from the converter), are rejected and the other end may then be examined. Upon selection of the electron track endpoint, the trajectory of the electron within the plane of the CCD is determined by identifying the ridge of the energy deposition distribution as a function of CCD position. The initial portion of the track is then used to determine α_r. Energy deposition during this initial portion of the track, ΔE, over a (projected) distance, ΔR, may then be used to determine β_r by comparing to an expected energy deposition rate, dE/ds.

$$\cos\beta_r = \frac{dE/ds}{\Delta E}\Delta R \tag{8}$$

The distribution of Δ_α and Δ_β are key to the performance of the system. Both distributions are centered about 0. Whereas Δ_β is so broad that the vertical reconstruction of electron positions rarely even lay on the passive converter, the width Δ_α indicates that if β could be determined by other means, α could be used effectively to determine characteristics of the scattered electrons and in turn the beam photons. The RMS widths of Δ_α, denoted σ_α, are plotted versus incidence angle, β, in Fig. 8. The figure indicates that 5 μm pixels perform slightly better than 10.5 μm pixels. Also, for back-plane irradiation, the diffusion that occurs during charge collection is an important aspect of the reconstruction and that 5°–8° α uncertainty is possible across a range of electron incident angles. If the simulations of electron tracks had included electronic noise, other work [45] has indicated that pixel sizes between 5 and 10 μm are likely optimal, because for smaller pixels, per-pixel noise in measured energy deposition begins to limit the fidelity of α angle determination.

Because the electron track reconstruction method was found to be ineffective at determining β, the converter was redesigned to be a 1-mm wide horizontal strip spanning across the entire collimated beam, rather than a slab or planar converter. In this way, β can be constrained simply through the geometry of the system.

The energy and position resolution of the reconstructed γ ray can be estimated by expanding Eq. (4) to account for position dependence of ϕ-resolution.

$$\sigma_{E_\gamma}^2 = \left(\frac{\partial E_\gamma}{\partial\alpha}\right)^2\sigma_\alpha^2 + \left(\frac{\partial E_\gamma}{\partial\beta}\right)^2\sigma_\beta^2 + \left(\frac{\partial E_\gamma}{\partial E_e}\right)^2\sigma_{E_e}^2. \tag{9}$$

$$\frac{\partial E_\gamma}{\partial\alpha} = \frac{m_e c^2\xi\sin\alpha\cos\beta}{(\xi\cos\alpha\cos\beta - 1)^2}, \tag{10}$$

$$\frac{\partial E_\gamma}{\partial\beta} = \frac{m_e c^2\xi\cos\alpha\sin\alpha}{(\xi\cos\alpha\cos\beta - 1)^2}, \tag{11}$$

and $\frac{\partial E_\gamma}{\partial E_e}$ was given in Eq. (5). Position-dependent contributions to the reconstructed γ-ray energy uncertainty due to uncertainties in α, $\frac{\partial E_\gamma}{\partial\alpha}\sigma_\alpha$, (from CCD tracking) and β, $\frac{\partial E_\gamma}{\partial\beta}\sigma_\beta$, (from geometric constraints of a 1 mm wide converter strip) are shown in Figs. 9 and 10, respectively. The values of σ_α are those shown in Fig. 8. For σ_β, the minimum and maximum allowable β values are determined by the distance to the converter strip, and σ_β is taken as $0.678w$, where w is the difference between the angular limits. This value is the RMS for a flat-top distribution of width w. These figures indicate that, except in the few-square-mm area nearest the converter, the α-uncertainty has a substantially larger impact on reconstructed photon energy resolution. This suggests that the height of passive converter (1 mm here) could be increased without substantially compromising resolution performance, while improving counting statistics. However, the height of the converter strip is also constrained by the distance over which the photon distribution varies, as shown in Fig. 1 such that 1 mm is a reasonable value for the current study.

The uncertainty in the measurement of the electron energy, σ_{E_C}, was estimated by combining two effects associated with CCD-based electron measurements; statistical noise and dark current. For statistical

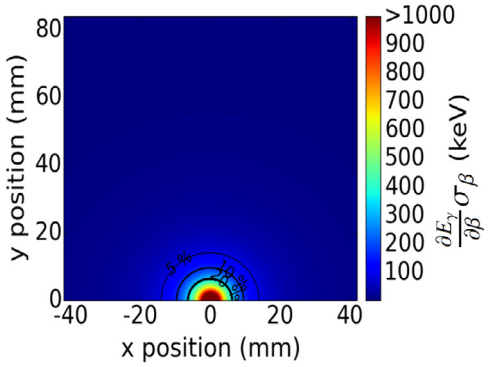

Fig. 10. Expected contribution to energy resolution due to β angular resolution for given electron incident position on the CCD assuming that β is constrained by a converter strip of 1 mm vertical span.

noise, the Fano factor, $f = 0.16$ and charge carrier liberation energy, $Q_l = 0.0037$ keV/pair, are used [46]. For dark current noise, CCD measurements demonstrated a per-pixel Gaussian noise distribution with a zero mean and a standard deviation, $\sigma_D = 0.0228$ keV. Tracks in the CCD due to electrons with higher energy tend to be longer resulting in noise from more pixels being summed during track energy determination. An approximate and heuristic relationship obtained from simulated electron tracks indicates that the number of pixels (per unit energy of the incident electron) into which energy is deposited scales roughly as $N_P[\#/\text{keV}] \approx 0.8\cos\beta - 0.12$. These energy resolution phenomena are combined as,

$$\sigma_{E_e} \approx \sqrt{f Q_l E_e} + \sigma_D / \sqrt{E_e(0.8\cos\beta - 0.12)}, \tag{12}$$

where E_e is given in keV.

The expected contribution to energy resolution due to measured electron energy uncertainties, $\frac{\partial E_\gamma}{\partial E_e}\sigma_{E_e}$, is plotted as a function of position incident upon the CCD in Fig. 11. The values indicated in the figure are substantially smaller than those in Figs. 9 and 10. This is fortunate, because there are other phenomena that may contribute to electron energy uncertainty that are of similar magnitude, but are less easy to quantify and have been omitted. Important phenomena that have been omitted from the electron energy uncertainty estimation include the possibility that the kinetic energy of the Compton electrons may not entirely be deposited within the sensitive volume of the electron tracker and that the electron track processing algorithm may fail to identify those electrons that escape. Individual CCD layers are capable of providing depth resolution through observation of depth-dependent diffusion. This resolution provides a means of identifying escaping electrons, but some electrons will unavoidably be mis-identified and others will produce secondary low-energy photons that may escape the tracker without providing attributable signals. Acknowledging this shortcoming, we assert that the scale of $\frac{\partial E_\gamma}{\partial E_e}$ is likely sufficiently small to not adversely impact the conclusions drawn herein.

The three components contributing to reconstructed γ-ray energy uncertainty are combined using Eq. (9), plotted as functions of position of Compton electron incidence upon the CCD, and shown as solid contours in Fig. 12. The figure indicates that there are roughly parabolic contours encapsulating areas of 5%, 10% and 35% of the CCD area where energy resolution of less than 5%, 10% and 20%, respectively can be achieved. Fig. 12 also shows the spatial resolution along the length of the converter strip for reconstructed γ rays as dashed contours within the tracker geometry. The spatial resolution is estimated as the product of the α angular resolution and the distance between the tracker and the scatterer, d. A position resolution of 3 mm and an energy resolution of 10% can be achieved in the same region. There is some spatial overlap between regions of the converter that perform well in terms of

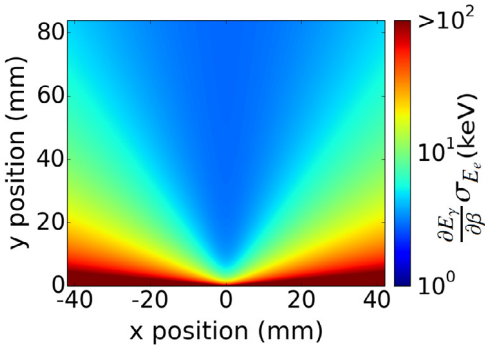

Fig. 11. Expected contribution to energy resolution due to measured electron energy uncertainties, $\frac{\delta E_\gamma}{\delta E_e}\sigma_{E_e}$, for given electron incident position on the CCD.

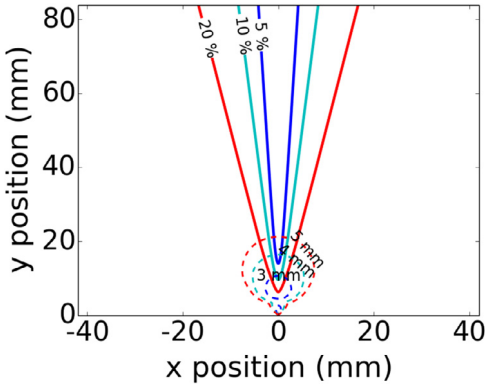

Fig. 12. Expected energy and position resolution contours for reconstructed γ rays as a function of incident position of converter-scattered Compton electrons upon the CCD.

spatial resolution and regions that perform well with respect to energy reconstruction, but in general, events producing small Compton electron scattering angles (ϕ_e) result in the best tracker energy performance and events that produce small d, which are typically associated with large β result in the best spatial performance. In the following it is examined how well a system could perform in the presence of these constraints by directly reconstructing each individual measured electron to populate a distribution of most probable energy–position pair reconstructions and then selecting the most probable beam based on that reconstructed distribution for each simulated shot.

6. Photon beam reconstruction and identification

Having obtained through modeling representations for the spatial and energy point-spread functions of the tracker system, we proceed to use the beam descriptions outlined in Section 2 as input source characteristics for further GEANT4 simulations. The sources were each simulated to propagate in vacuum, through a perfect collimator that has a semi-circular, 10-mm diameter opening, prior to impinging upon a nitrocellulose scatterer film with 10 mm (horizontal) and 1 mm (vertical) dimensions and thicknesses ranging from 15 to 40 μm. The collimator was chosen to be semi-circular to minimize the vertical distance between Compton electrons produced in the converter and the first CCD layer in the tracker. A stack of four tracker CCDs, each spaced by 3 mm were simulated. The top face of the first CCD was placed 3.5 mm below the center of the beam line, which would be within the beam, were the collimator circular. Energy depositions within each CCD were registered, and diffusion and electron track reconstruction algorithms were applied in post-processing, as described above. A

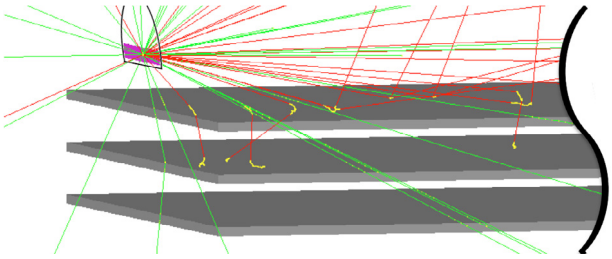

Fig. 13. GEANT4 model of the scatter–tracker diagnostic system. The converter strip is visible as a magenta rectangle, photons incident upon the scatterer are not shown, but scattered photons are green. Compton scattered electrons traveling in vacuum are red and positions where energy deposition occur are shown as yellow. Three CCD layers have been rendered and are shown in gray. The semi-circular collimator opening is also shown in black. (For interpretation of the references to color in this figure legend, the reader is referred to the web version of this article.)

rendering of most of the simulated geometry is shown in Fig. 13. Note that while the majority of CCD interactions are due to Compton electrons, scattered photons are also capable of producing signals within the CCD. The effects of these scattered photons are taken into account in our simulations, although they are nearly negligible due to the selection criteria imposed by the electron track reconstruction algorithm.

For each beam, 5×10^3 sets of simulations that would each represent 10^8 photons through a 1-cm diameter circular collimator were conducted, where each set is considered to represent a single shot. Although the number varies from beam to beam, approximately 15% of a set's photons impinge upon the converter strip. For each shot, on average, 120 electrons per micron of converter thickness are produced in the scatter, and about half of those are incident upon the first layer of the CCD tracker. Of Compton electrons incident upon the tracker, 51% escape from the top of the CCD without depositing the entirety of their kinetic energy. 35% of the Compton electrons deposit all their energies in the first layer, 7% stop in the second layer, 2% in the third layer, and 0.5% in the fourth. The remainder of the electrons incident upon the tracker escape from the space between the CCDs. Given how little additional information is obtained from the 3rd and 4th layers, a two-layer tracker appears to be most reasonable and is solely considered hereafter.

For a given photon beam, the photon distribution incident upon the converter strip is extracted from the simulations described in Section 2. Such a distribution is shown for the nominal beam in Fig. 14a. Thereafter, the effects of the converter and the tracker are taken into account via the GEANT4 simulations and through post processing as described in Section 5. These steps create, for each Compton electron that interacts within the tracker and that is not rejected by the track selection algorithms, the most probable γ-ray energy and interaction position, x_r. These values can then be histogrammed for a shot or across all shots. The average reconstructed beam profile across all 5×10^3 simulated shots for the nominal beam incident upon a 15 μm-thick converter is shown as Fig. 14b. Thereafter, reconstructed beam profiles of the simulated beam can be modeled by sampling the population of each bin. For each bin, the mean number of reconstructed events observed from the 5×10^3 simulated shots is treated as the mean of a Poisson distribution that is sampled to determine the population in each bin from a single beam shot. The dimensions of the bins that produce the best performance are a trade-off; larger bins result in better statistics at the expense of position and energy resolution loss. An example of a sampled reconstructed single shot of the nominal beam using this Poisson method and for bin widths of 200 keV in reconstruction energy and 2.5 mm in reconstructed position is shown as Fig. 14c. Clearly, even with the indicated coarse binning structure, statistical variability is evident within this reconstruction.

Table 3
Confusion matrix showing probability of classifying an observed beam, derived from a Poisson-sampling of mean reconstructed beams, using the binning structure that demonstrated the best performance (Δx_r = 2.5 mm and Δe_r = 250 keV), and based upon a set of four beams with differing electron angular spreads and a 30 μm-thick nitrocellulose converter.

		Predicted dθ (mrad)			
		0.19	0.43	0.86	1.75
True	0.19	0.92	0.08	0	0
	0.43	0.18	0.81	0.01	0
	0.86	0	0.05	0.91	0.04
	1.75	0	0	0.05	0.95

The nominal photon beam ($d\theta$ = 0.19 mrad and $\Delta E_e^B / E_e^B$ = 4.5%) and beams that have larger electron angular spreads ($d\theta$ = 0.43, 0.84, and 1.75 mrad) were simulated, reconstructed, and then Poisson-sampled to reproduce reconstructions of individual 10^8-photon shots. Example profiles for these three beams as they are modeled through the three steps are shown in Fig. 15. For each simulated reconstruction, i, the number of events, $N^i_{e_r,x_r}$ reconstructed to populate each bin, (denoted by e_r and x_r), is compared to the mean number of events from each of the three simulated angular spread beams, $\bar{N}_{e_r,x_r}$. The beam that produces the smallest value of,

$$\chi^2 = \sum_{e_r} \sum_{x_r} (N^i_{e_r,x_r} - \bar{N}_{e_r,x_r})^2 \tag{13}$$

is selected as the most probable beam. This process, referred to herein as a χ^2 comparison, was performed 10^3 times each for different histogram bin sizes and for converter thicknesses of 15, 20, 30 μm. Fig. 16 shows in red the mean true probability for selecting the correct distribution across the four varying angular-spread beams for 30 μm-thick converters. In all cases, thicker converters demonstrated better performance. This motivated simulation of 40 and 50 μm converter thicknesses, which also demonstrated improved performance in the χ^2 comparison beam unfolding method, but the findings in Section 3 and the discussion below indicate that pursuing increased converter thicknesses may not result in the same level of performance improvement as improving beam unfolding logic. The simulations also indicated probabilities of electron tracks overlapping as 1%, 1.5%, 1.8% and 2.2% for 20, 30, 40 and 50 μm scatter film thicknesses, respectively.

Bin widths, for x_r and e_r near 2 mm and 100–250 keV resulted in the best performance. The highest mean true positive rate for the simulated set of beams of varying $d\theta$ classifications was 90 ± 1% for Δx_r = 2.5 mm and Δe_r = 250 keV using the 30 μm-thick converter. The confusion matrix for comparing these three beams, using the binning with the best-observed performance is shown in Table 3.

Similarly, the response in the proposed diagnostic system of the nominal beam and beams that have larger electron energy spreads ($\Delta E_e^B / E_e^B$ = 12 and 24% FWHM) were compared and the highest mean true positive rate for this simulated set of beam classifications was 83 ± 1% for Δx_r = 2.5 mm and Δe_r = 150 keV. The confusion matrix for these beams, this binning, and a 30 μm-thick converter is shown in Table 4. As one might expect, the *edge cases* (where only one simulated beam is adjacent in the considered parameter space) demonstrate better performance, but even for beams where multiple false positives are plausible, the simulations suggest true positive rates of greater than 70%.

The responses of all six simulated beams (i.e., the nominal beam, two other energy-spread beams and three other angular spread beams) within the diagnostic system were also compared in a single analysis. The resulting confusion matrix is shown in Table 5. While some additional misclassification occurs when additional beams are compared, the average overall recall remains 85%.

7. Discussion

Section 5 indicated that the fidelity with which individual photons can be reconstructed depends on both the angle of Compton scatter, ϕ_e

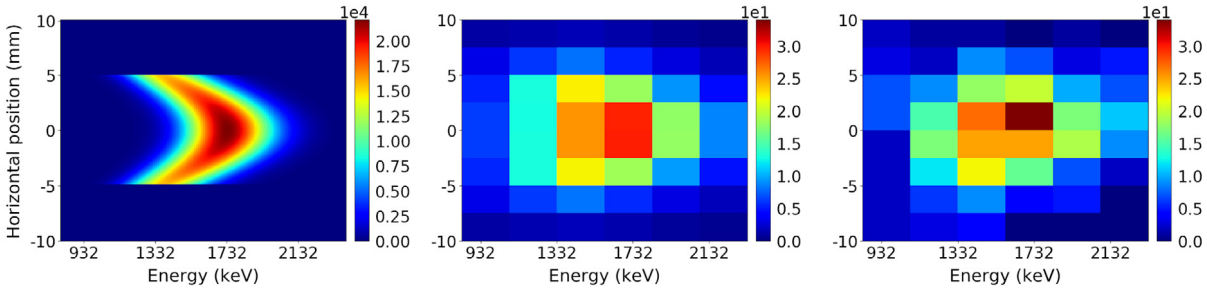

Fig. 14. (a) Profile incident upon the 1-mm height scatter strip of a photon beam produced by head-on scattering of an 800-nm laser with an electron beam having 0.19 mrad angular spread and 4.5% energy spread (i.e., the nominal beam). The beam is simulated as 10^8 photons through the collimator, which results in 1.6×10^7 photons incident upon the scatterer. Color axis dimensions are photons/mm/keV for a single shot from the average of 5×10^3 shots. (b) Mean simulated reconstruction of the beam shown in (a) incident upon a 15μm-thick converter and tracked using a two-layer CCD system. The histogram dimensions are 200 keV and 2.5 mm in reconstructed energy and photon interaction position, respectively. The color scale units are number of reconstructed events per shot. (c) A Poisson-sampling of a single-shot beam reconstruction using same units as (b).

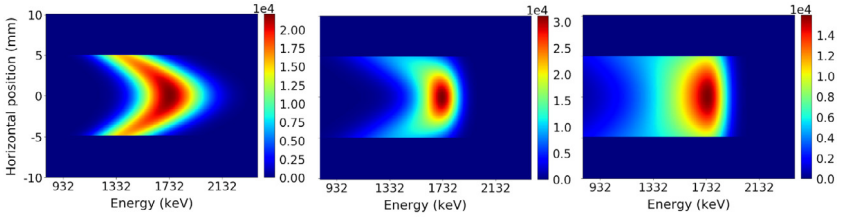

(a) Photon beam profiles incident upon the converter produced by electron beams having angular spreads of 0.19 mrad(left), 0.43 mrad(middle) and 0.84 mrad(right)

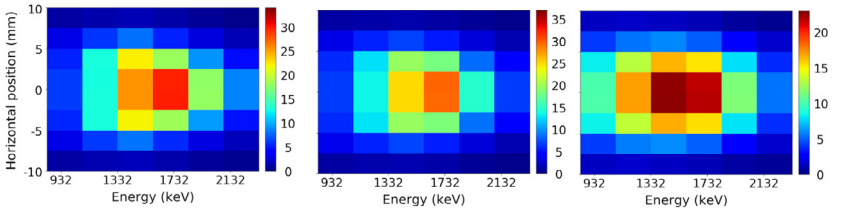

(b) Average reconstructed profiles from 5×10^3 simulations a single shot of the beams shown in (a) incident upon a 15 μm converter.

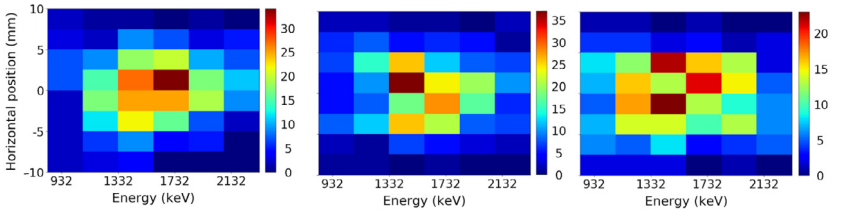

(c) Examples of reconstructed profiles from a single simulated shot of the beams shown in (a) incident upon a 15 μm converter.

Fig. 15. Photon beam with varying angular spreads and their reconstructions. For (a) and (b) the profiles are the same as those shown in 14, whereas (c) represents a different statistical sampling.

(and resulting E_e), and on the incidence angle of the Compton electron, relative to the CCD surface plane, β. These combined phenomena result in the energy and spatial resolution for a pencil beam incident upon the converter that is shown in Fig. 12. Through modeling, Section 6 then demonstrated the approximate 'beam-type resolution' that could be achieved by simply minimizing the residuals between the histogrammed observed reconstructed beam relative to the mean beam. This method achieved approximately 90% recall, or appropriate beam identification when selecting between beams that differed by factors of two (between adjacent beams) in beam electron energy spread (ΔE_e^b) or that differed by factors of 2–4 in beam electron energy spread ($d\theta$). The performance varied with histogram dimensions (Δx_r and Δe_r), where the resolution within the tracker is sacrificed to improve statistics within each histogram bin. While this modeling indicates that this χ^2 beam selection method will provide a valuable capability for performing diagnostic measurements of laser-Compton produced photon beams, it appears that

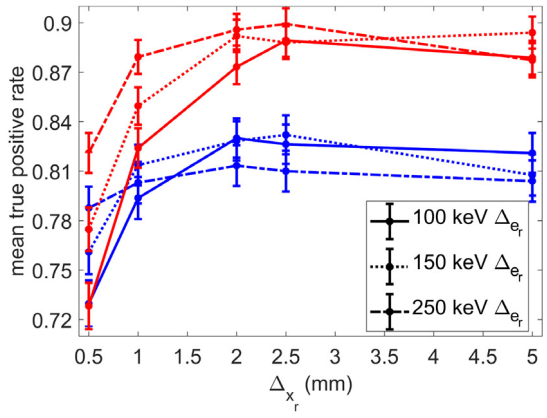

Fig. 16. True positive probabilities for χ^2-comparisons of four beams of varying angular spread (red) and three beams of varying energy spread (blue) incident upon a 30 μm-thick converter versus reconstructed histogram position bin width, Δx_r, for three reconstructed energy bin widths, Δe_r indicated in the legend. (For interpretation of the references to color in this figure legend, the reader is referred to the web version of this article.)

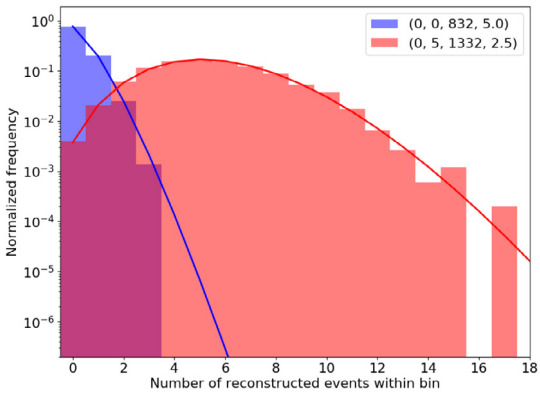

Fig. 17. Example frequency distributions for two reconstruction-space bins for the nominal beam incident upon the 30 μm converter. The bins are labeled in the legend through the lower limit of the beam in x, y, e_r, and x_r, respectively. Also shown as lines are the distribution mean-based Poisson fits for the two bins.

Table 4
Confusion matrix for classifying beams between three different electron energy spreads with binning structure $\Delta x_r = 2.5$ mm and $\Delta e_r = 150$ keV using a 30 μm-thick nitrocellulose converter.

		Predicted $\Delta E_e^B/E_e^B$(%)		
		4.5	12	24
True	4.5	0.81	0.19	0
	12	0.16	0.72	0.12
	24	0	0.03	0.97

Table 5
Confusion matrix for classifying all six simulated beams with binning structure $\Delta x_r = 2.5$ mm and $\Delta e_r = 250$ keV using a 30 μm-thick nitrocellulose converter. Labels are for pairs of beam parameters, $\Delta E_e^B/E_e^B$ and $d\theta$.

		Predicted Beam					
	$\Delta E_e^B/E_e^B$(%)	24%	12%	4.5%	4.5%	4.5%	4.5%
	$d\theta$	0.19	0.19	0.19	0.43	0.84	1.75
True	24%, 0.19	0.90	0.03	0	0.03	0.04	0
	12% ,0.19	0.03	0.71	0.12	0.14	0	0
	4.5%, 0.19	0	0.09	0.86	0.05	0	0
	4.5%, 0.43	0.02	0.12	0.06	0.78	0.02	0
	4.5%, 0.84	0.03	0	0	0.02	0.92	0.03
	4.5%, 1.75	0	0	0	0	0.05	0.94

methods of reconstructing the incident beam that utilize knowledge of the position-dependent resolution of the tracker could further improve performance.

A first attempt at leveraging additional knowledge was made, wherein the reconstructions of all simulated photons described in Section 6 (i.e., the 5×10^3 simulations of a beam shot for each of the seven beams) were used to populate a more finely discretized space. Specifically, the reconstructed events from each Compton electron track were histogrammed into the same reconstructed energy and track position bins ($\Delta x_r = 2.5$ mm and $\Delta e_r = 250$ keV) but also into 5 mm × 5 mm spatial bins of incident position upon the CCD. To be clear, the reconstructed events from each shot were histogrammed into four dimensions, rather than just the two shown in Section 6. 80% of the shots were selected randomly to be used for training and the remaining 20% were reserved for testing. Using the training set for each beam, the number of reconstructed events that fell within each bin was tallied for each shot. Frequency distributions were generated for each bin across all $4{\times}10^3$ training shots for each beam. Examples of such distributions are shown as histograms for two bins in the four-space in Fig. 17. The mean values of these distributions obtained from the simulations were treated as the true mean values of Poisson probability functions for each bin in the 4-space and for each of the six simulated beams. The remaining 10^3 test shots for each of the beams were then reconstructed and binned into the four dimensions. A probability score for assigning the ith simulated test beam to η type of beam is determined as,

$$P^{i,\eta} = \prod_b exp(-\lambda_b^\eta)\frac{(\lambda_b^\eta)^{k_b^i}}{k_b^i!}, \tag{14}$$

where λ_b^η is the fit Poisson mean for each bin, b, and k_b^i is the observed number of events for the ith shot reconstructed into bin b. The beam that produces the highest value for $P^{i,\eta}$ is selected as a most probable beam. This *Poisson probability maximization* beam selection method has not been subjected to an optimization study to identify the optimal bin sizes, but with the binning described above, the true positive rates described in Table 4 improve to 88, 83, and 96% for the 4.5, 12, and 24% $\Delta E_e^b/E_e^b$ beams, respectively. Similarly, the performance for the $d\theta$ beams all improve, with recall for the $d\theta = 0.43$ mrad beam showing the most marked improvement up to 90%.

It was also observed that for the χ^2 beam selection method, thicker converters produced better results, owing to the increased numbers of converted electrons, despite the findings shown in Table 1 that each converted electron is more likely to have undergone sufficient scattering to generate appreciable additional uncertainty in the reconstruction of the measured photon energy (the 2% metric is shown). It would therefore be expected that better performance across the same beams or comparable performance when comparing between more similar beams could be achieved if more converted electrons could be generated. Possible means of accomplishing this include increasing the height of the converter, or using multiple converter/tracker stages to obtain better sampling of the beam. The comparison between σ_α and σ_β contributions to reconstructed energy uncertainty indicate that the former could be done with little performance impact, although sampling a larger spatial extent of the beams shown in Fig. 1 would introduce additional spatial ambiguity in the measurement. Using multiple diagnostic stages would likely result in a significantly more complex experimental set up, but the only technical hurdle would be ensuring sufficient shielding between stages.

8. Conclusions

This paper has presented a design for a radiation detection system to be used as a diagnostic for measuring laser-Compton scatter-produced photon beams in a single, nearly instantaneous shot. This is particularly valuable for LCS beams where the electron beam is accelerated within a plasma laser wakefield. In such a process, due to the low repetition rate

of near-term experiments, a diagnostic capable of inferring the electron beam properties from a single shot is highly desired. Given the physics of photon interactions with matter and electron stopping, few direct measurements of such beams are feasible. While magnetic spectrometers and gaseous trackers are also potentially useful, we have presented here a diagnostic based on a passive converter material that scatters beam photons and a CCD-based out-of-beam tracker that measures the resulting Compton electrons.

This paper has shown results of simulations that indicate that photon beams generated by relativistic electron energies of 270 MeV and spreads of 4.5, 12, and 24% FWHM can be distinguished with 75%–95% probability; similarly that photon beams generated from electron beams with angular spreads of $d\theta = 0.19$, 0.43, 0.86 and 1.75 mrad can be distinguished with 90% probability; and that distinguishing the set of all six simulated beams resulted in average recall of 85%. The peak areal intensity of the nominal simulated photon beam is at 1.7 MeV, and the FWHM energy spread near the center of the beam is 10%. At regions outside the beam centroid, the peak intensity shifts to lower energies resulting in an energy profile that is both broadened and down-shifted, as indicated in Fig. 2. The beams of increased $d\theta$ present similar area-integrated energy distributions to the nominal beam, but show less variation in energy distributions across different angular slices than the nominal beam. Conversely, for the beams of increased ΔE_e^B, the energy spreads of the resulting photon beams are increased while the variation in energy with angle remain more consistent. Whereas the centroid FWHM energy spread of the nominal beam was 10%, it is 25% and 50% for the $\Delta E_e^B / E_e^B = 10$ and 20%, respectively.

The fact that the simulated diagnostic, combined with the χ^2 analysis method performed better in distinguishing the differing $d\theta$ beams is noteworthy. Spectroscopically, the varying energy-spread beams differ more substantially than the differing $d\theta$ beams. However, it appears that this spectral variation is not well resolved due to the wide binning required to provide an optimal compromise between reducing statistical fluctuations and maintaining position and energy resolution. This suggests that the Poisson probability maximization method could better take advantage of smaller bin sizes. Bin dimensions could also vary in size according to where on the CCD a tracked electron was incident such that regions with good spatial resolution have smaller x_r bins and those regions better energy resolution have smaller e_r bins, thereby likely achieving better compromises between resolution and statistics. More complex beam analysis methods could also be brought to bear, such as using the modeling-derived resolution functions to directly reconstruct the most probable beam, or to use that reconstruction to select from a set of hypothesized beams.

The presented beam diagnostic design has assumed that the beam is centered vertically relative to the horizontal passive converter. We assert that a simple integrating beam imager, such as a phosphor screen positioned further downstream could confirm relative spatial alignment. Whether the methods described here could be further applied to misaligned beams should be studied further, but the assumption of correct alignment can likely be experimentally confirmed without influencing these measurements.

Despite the expectation that the beam classification methods could be improved to provide better selectivity, or comparable selectivity across more similar beams, it is noteworthy that by using the simple 2D χ^2 method, acceptable performance appears probable. This method has only been optimized across the two dimensions of the reconstruction bins and in the simulations described herein, thicker converters have continued to suggest better performance. Improving the beam classification criterion is anticipated to have sufficiently large impacts on performance, which is why simulations and optimizations of increased converter thickness have been put aside until further study of the former. This study will continue to explore modern computer-driven classification methods as well as more statistical approaches.

Another aspect that should be highlighted is construction of such a diagnostic system. Ref. [31] showed results from measurements performed with a CCD of the type described here measuring ^{60}Co, ^{88}Y, and ^{241}Am. While the electron tracking capabilities with the CCD have been well studied in Ref. [44], analysis of the data summarized in Ref. [31] indicate that those capabilities can be improved upon. This possibility is due to the fact that in the proposed geometry, electrons are incident upon the surface of the CCD, rather than being created via Compton scatter within the bulk of the device. This additional knowledge can be leveraged to design an electron tracking algorithm that we anticipate would outperform the algorithm used in this work. Such tracking algorithm work will be the subject of future study.

The CCD systems that have been chosen for performing the diagnostic measurement have some depth resolution due to differences in the diffusive spread of charge that is observed for differing depths within the CCD that the energetic electrons induce charge liberation. This allows us, with some confidence to distinguish between tracks that end within the CCD versus those that escape the Si volume. The depth resolution of the CCDs is better on pixel side, which enables our design to include two back-to-back CCD trackers that have good depth resolution at the top and bottom. This configuration should result in the best performance in determining whether electrons escape the tracker. This configuration also allows for the two CCD tracker layers to be placed very close together, which facilitates correlating electron tracks across the layers. Practically, a design with two CCD layers requires substantially less engineering than incorporating a third layer. The wires connections for the CCD readout require several mm of vertical clearance, but by positioning two CCDs back-to-back, clearance is not an issue.

We therefore plan to begin building the proposed diagnostic system and anticipate that by applying the χ^2 beam selection method described in this paper we will be able to distinguish between beams that vary in energy and/or angular spread by factors of two. Development and refinement of better beam selection/reconstruction methods will be the subject of further study. Also, by directly imaging individual Compton-scattered electrons, we anticipate making the first simultaneous measurements of both spatial profile and energy of an MeV-scale LCS beam.

Acknowledgments

This work was supported by the U.S. Dept. of Energy National Nuclear Security administration Defense Nuclear Nonproliferation R&D (NA-22), and by the Office of Science under Contract No. DE-AC02-05CH11231. We would like to acknowledge initial design discussions with Dan Chivers, Lucian Mihailescu, and Ren Cooper, and Changchun Sun for providing us and instructing us on the use of the CCSC code.

References

[1] J. Pruet, D.P. McNabb, C.A. Hagmann, F.V. Hartemann, C.P.J. Barty, Detecting clandestine material with nuclear resonance fluorescence, J. Appl. Phys. 99 (12) (2006) 123102. http://dx.doi.org/10.1063/1.2202005. arXiv:https://doi.org/10.1063/1.2202005.

[2] C. Geddes, B. Ludewigt, J. Valentine, B. Quiter, M.-A. Descalle, G. Warren, M. Kinlaw, S. Thompson, D. Chichester, C. Miller, S. Pozzi, Impact of monoenergetic photon sources on nonproliferation applications, Tech. rep., DNN R & D final project report, 2017, http://dx.doi.org/10.2172/1376659. http://www.osti.gov/scitech/servlets/purl/1376659.

[3] B. Quiter, T. Laplace, B. Ludewigt, Examining ^{239}Pu and ^{240}Pu nuclear resonance fluorescence measurements on spent fuel for nuclear safeguards, in: Proceedings of the 53rd Annual Meeting of the Institute of Nuclear Materials Management 2012 53, 2012.

[4] C. Angell, T. Hayakawa, T. Shizuma, R. Hajima, Significant improvemetn of nuclear fluorescence non-destructive assay by using the average resonance technique and photofission, in: Proceedings of the 53rd Annual Meeting of the Institute of Nuclear Materials Management 2012 53, 2012.

[5] J. McFee, A. Faust, K. Pastor, Photoneutron spectroscopy using monoenergetic gamma rays for bulk explosives detection, Nucl. Instrum. Methods Phys. Res. A 704 (2013) 131–139. http://dx.doi.org/10.1016/j.nima.2012.12.053. URL http://www.sciencedirect.com/science/article/pii/S0168900212015860.

[6] W. Hendrickson, Determination of macromolecular structures from anomalous diffraction of synchrotron radiation, Science 254 (5028) (1991) 51–58. http://dx.doi.org/10.1126/science.1925561. arXiv:http://science.sciencemag.org/content/254/5028/51.full.pdf. URL http://science.sciencemag.org/content/254/5028/51.

[7] B. Dietz, H. Weidenmüller, Photonuclear reactions induced by intense short laser pulses, Phys. Lett. B 693 (3) (2010) 316–322. http://dx.doi.org/10.1016/j.physletb.2010.07.061. URL http://www.sciencedirect.com/science/article/pii/S0370269310010130.

[8] R. Schützhold, H. Gies, G. Dunne, Dynamically assisted Schwinger mechanism, Phys. Rev. Lett. 101 (2008) 130404. http://dx.doi.org/10.1103/PhysRevLett.101.130404. URL https://link.aps.org/doi/10.1103/PhysRevLett.101.130404.

[9] H.R. Weller, M.W. Ahmed, H. Gao, W. Tornow, Y.K. Wu, M. Gai, R. Miskimen, Research opportunities at the upgraded higs facility, Prog. Part. Nucl. Phys. 62 (1) (2009) 257–303. http://dx.doi.org/10.1016/j.ppnp.2008.07.001. URL http://www.sciencedirect.com/science/article/pii/S0146641008000434.

[10] S.G. Rykovanov, C.G.R. Geddes, J.-L. Vay, C.B. Schroeder, E. Esarey, W.P. Leemans, Quasi-monoenergetic femtosecond photon sources from thomson scattering using laser plasma accelerators and plasma channels, J. Phys. B: At. Mol. Opt. Phys. 47 (23) (2014) 234013. URL http://stacks.iop.org/0953-4075/47/i=23/a=234013.

[11] ATF, Accelerator test facility facts, 2014. https://www.bnl.gov/bnlweb/pubaf/fact_sheet/pdf/FS-ATF.pdf. (Accessed 6 April 2018).

[12] O. Tesileanu, D. Ursescu, R. Dabu, N.V. Zamfir, Extreme light infrastructure – nuclear physics, J. Phys. Conf. Ser. 420 (1) (2013) 012157. URL http://stacks.iop.org/1742-6596/420/i=1/a=012157.

[13] C. Sun, J. Li, G. Rusev, A.P. Tonchev, Y.K. Wu, Energy and energy spread measurements of an electron beam by compton scattering method, Phys. Rev. ST Accel. Beams 12 (2009) 062801. http://dx.doi.org/10.1103/PhysRevSTAB.12.062801. URL https://link.aps.org/doi/10.1103/PhysRevSTAB.12.062801.

[14] F. Albert, S.G. Anderson, D.J. Gibson, C.A. Hagmann, M.S. Johnson, M. Messerly, V. Semenov, M.Y. Shverdin, B. Rusnak, A.M. Tremaine, F.V. Hartemann, C.W. Siders, D.P. McNabb, C.P.J. Barty, Characterization and applications of a tunable, laser-based, MeV-class Compton-scattering γ-ray source, Phys. Rev. ST Accel. Beams 13 (2010) 070704. http://dx.doi.org/10.1103/PhysRevSTAB.13.070704. URL https://link.aps.org/doi/10.1103/PhysRevSTAB.13.070704.

[15] H. Schwoerer, B. Liesfeld, H.-P. Schlenvoigt, K.-U. Amthor, R. Sauerbrey, Thomson-backscattered x rays from laser-accelerated electrons, Phys. Rev. Lett. 96 (2006) 014802. http://dx.doi.org/10.1103/PhysRevLett.96.014802. URL https://link.aps.org/doi/10.1103/PhysRevLett.96.014802.

[16] K. Khrennikov, J. Wenz, A. Buck, J. Xu, M. Heigoldt, L. Veisz, S. Karsch, Tunable all-optical quasimonochromatic thomson x-ray source in the nonlinear regime, Phys. Rev. Lett. 114 (2015) 195003.

[17] A. Jochmann, A. Irman, M. Bussmann, J.P. Couperus, T.E. Cowan, A.D. Debus, M. Kuntzsch, K.W.D. Ledingham, U. Lehnert, R. Sauerbrey, H.P. Schlenvoigt, D. Seipt, T. Stöhlker, D.B. Thorn, S. Trotsenko, A. Wagner, U. Schramm, High resolution energy-angle correlation measurement of hard x rays from laser-thomson backscattering, Phys. Rev. Lett. 111 (2013) 114803. http://dx.doi.org/10.1103/PhysRevLett.111.114803. URL https://link.aps.org/doi/10.1103/PhysRevLett.111.114803.

[18] S. Chen, N.D. Powers, I. Ghebregziabher, C.M. Maharjan, C. Liu, G. Golovin, S. Banerjee, J. Zhang, N. Cunningham, A. Moorti, S. Clarke, S. Pozzi, D.P. Umstadter, Mev-energy x rays from inverse compton scattering with laser-wakefield accelerated electrons, Phys. Rev. Lett. 110 (2013) 155003. http://dx.doi.org/10.1103/PhysRevLett.110.155003. URL https://link.aps.org/doi/10.1103/PhysRevLett.110.155003.

[19] K. Phuoc, S. Corde, C. Thaury, V. Malka, A. Tafzi, J.P. Goddet, R.C. Shah, S. Sebban, A. Rousse, All-optical compton gamma-ray source, Nat. Photonics 6 (2012) 308.

[20] N.D. Powers, I. Ghebregziabher, G. Golovin, C. Liu, S. Chen, S. Banerjee, J. Zhang, D.P. Umstadter, Quasi-monoenergetic and tunable x-rays from a laser-driven compton light source, Nat. Photonics 8 (2014) 28–31.

[21] H.-E. Tsai, X. Wang1, J.M. Shaw, Z. Li, A.V. Arefiev, X. Zhang, R. Zgadzaj, W. Henderson, V. Khudik, G. Shvets, M.C. Downer, Compact tunable compton x-ray source from laser-plasma accelerator and plasma mirror, Phys. Plasmas 22 (2015) 023106.

[22] C. Yu, R. Qi, W. Wang, J. Liu, W. Li, C. Wang, Z. Zhang, J. Liu, Z. Qin, M. Fang, K. Feng, Y. Wu, Y. Tian, Y. Xu, F. Wu, Y. Leng, X. Weng, J. Wang, F. Wei, Y. Yi, Z. Song, R. Li, Z. Xu, Ultrahigh brilliance quasi-monochromatic mev γ-rays based on self-synchronized all-optical compton scattering, Sci. Rep. 6 (2016) 29518. URL http://dx.doi.org/10.1038/srep29518.

[23] G. Tiwari, L. Lisi, C. Geddes, B.M. Hegelich, Personal communication.

[24] G. Sarri, D.J. Corvan, W. Schumaker, J.M. Cole, A. Di Piazza, H. Ahmed, C. Harvey, C.H. Keitel, K. Krushelnick, S.P.D. Mangles, Z. Najmudin, D. Symes, A.G.R. Thomas, M. Yeung, Z. Zhao, M. Zepf, Ultrahigh brilliance multi-MeV γ-ray beams from nonlinear relativistic thomson scattering, Phys. Rev. Lett. 113 (2014) 224801. http://dx.doi.org/10.1103/PhysRevLett.113.224801. URL https://link.aps.org/doi/10.1103/PhysRevLett.113.224801.

[25] W. Schumaker, G. Sarri, M. Vargas, Z. Zhao, K. Behm, V. Chvykov, B. Dromey, B. Hou, A. Maksimchuk, J. Nees, V. Yanovsky, M. Zepf, A.G.R. Thomas, K. Krushelnick, Measurements of high-energy radiation generation from laser-wakefield accelerated electron beams, Phys. Plasmas 21 (5) (2014) 056704. http://dx.doi.org/10.1063/1.4875336. arXiv:https://doi.org/10.1063/1.4875336. URL https://doi.org/10.1063/1.4875336.

[26] C. S, M.R. Islam, B. Ersfeld, R. Shanks, B. E, G. Vieux, X. Yang, R.I. et al., Gamma-rays from harmonically resonant betatron oscillations in a plasma wake, Nat. Phys. 7 (2011) 867–871. http://dx.doi.org/10.1038/nphys2090.

[27] D.J. Corvan, G. Sarri, M. Zepf, Design of a compact spectrometer for high-flux mev gamma-ray beams, Rev. Sci. Instrum. 85 (6) (2014) 065119. http://dx.doi.org/10.1063/1.4884643. arXiv:https://doi.org/10.1063/1.4884643.

[28] A.E. Gehring, M.A. Espy, T.J. Haines, J. Mendez, D.C.M. et al., Measuring x-ray spectra of flash radiographic sources, in: Proc. SPIE 9595, Radiation Detectors: Systems and Applications XVI, 959506, SPIEDigitalLibrary, 2015. http://dx.doi.org/10.1117/12.2188829.

[29] A.E. Gehring, M.A. Espy, T.J. Haines, J.F. Hunter, N.S.P. K., Determining x-ray spectra of radiographic sources with a compton spectrometer, in: Proc. SPIE 9215, Radiation Detectors: Systems and Applications XV, 921508, SPIEDigitalLibrary, 2014. http://dx.doi.org/10.1117/12.2065588.

[30] J.M. Cole, K.T. Behm, E. Gerstmayr, T.G. Blackburn, J.C. Wood, C.D. Baird, M.J. Duff, C. Harvey, A. Ilderton, A.S. Joglekar, K. Krushelnick, S. Kuschel, M. Marklund, P. McKenna, C.D. Murphy, K. Poder, C.P. Ridgers, G.M. Samarin, G. Sarri, D.R. Symes, A.G.R. Thomas, J. Warwick, M. Zepf, Z. Najmudin, S.P.D. Mangles, Experimental evidence of radiation reaction in the collision of a high-intensity laser pulse with a laser-wakefield accelerated electron beam, Phys. Rev. X 8 (2018) 011020. http://dx.doi.org/10.1103/PhysRevX.8.011020. URL https://link.aps.org/doi/10.1103/PhysRevX.8.011020.

[31] Y. Zhang, P.J. Barton, B.J. Quiter, K. Vetter, C.G.R. Geddes, A Geant4 simulation framework for the optimization of a CCD-based diagnostics for next generation photon sources, in: IEEE Nuclear Science Symposium, IEEE, 2015.

[32] Y. Zhang, B. Quiter, K. Vetter, C. Geddes, Diagnosing laser plasma accelerator based thomson source in a single shot by using CCD electron trackers, in: IEEE Nuclear Science Symposium, IEEE, 2016.

[33] S. Agostinelli, J. Allison, K. Amako, J. Apostolakis, H. Araujo, P. Arce, M. Asai, D. Axen, S. Banerjee, G. Barrand, F. Behner, L. Bellagamba, J. Boudreau, L. Broglia, A. Brunengo, H. Burkhardt, S. Chauvie, J. Chuma, R. Chytracek, G. Cooperman, G. Cosmo, P. Degtyarenko, A. Dell'Acqua, G. Depaola, D. Dietrich, R. Enami, A. Feliciello, C. Ferguson, H. Fesefeldt, G. Folger, F. Foppiano, A. Forti, S. Garelli, S. Giani, R. Giannitrapani, D. Gibin, J.G. Cadenas, I. Gonzlez, G.G. Abril, G. Greeniaus, W. Greiner, V. Grichine, A. Grossheim, S. Guatelli, P. Gumplinger, R. Hamatsu, K. Hashimoto, H. Hasui, A. Heikkinen, A. Howard, V. Ivanchenko, A. Johnson, F. Jones, J. Kallenbach, N. Kanaya, M. Kawabata, Y. Kawabata, M. Kawaguti, S. Kelner, P. Kent, A. Kimura, T. Kodama, R. Kokoulin, M. Kossov, H. Kurashige, E. Lamanna, T. Lampn, V. Lara, V. Lefebure, F. Lei, M. Liendl, W. Lockman, F. Longo, S. Magni, M. Maire, E. Medernach, K. Minamimoto, P.M. de Freitas, Y. Morita, K. Murakami, M. Nagamatu, R. Nartallo, P. Nieminen, T. Nishimura, K. Ohtsubo, M. Okamura, S. O'Neale, Y. Oohata, K. Paech, J. Perl, A. Pfeiffer, M. Pia, F. Ranjard, A. Rybin, S. Sadilov, E.D. Salvo, G. Santin, T. Sasaki, N. Savvas, Y. Sawada, S. Scherer, S. Sei, V. Sirotenko, D. Smith, N. Starkov, H. Stoecker, J. Sulkimo, M. Takahata, S. Tanaka, E. Tcherniaev, E.S. Tehrani, M. Tropeano, P. Truscott, H. Uno, L. Urban, P. Urban, M. Verderi, A. Walkden, W. Wander, H. Weber, J. Wellisch, T. Wenaus, D. Williams, D. Wright, T. Yamada, H. Yoshida, D. Zschiesche, Geant4 – a simulation toolkit, Nucl. Instrum. Methods Phys. Res. A 506 (3) (2003) 250–303. http://dx.doi.org/10.1016/S0168-9002(03)01368-8. URL http://www.sciencedirect.com/science/article/pii/S0168900203013688.

[34] C. Sun, Y. Wu, G. Rusev, A. Tonchev, End-to-end spectrum reconstruction method for analyzing compton gamma-ray beams, Nucl. Instrum. Methods Phys. Res. A 605 (3) (2009) 312–317. http://dx.doi.org/10.1016/j.nima.2009.03.237. URL http://www.sciencedirect.com/science/article/pii/S0168900209007359.

[35] E. Bulyak, V. Skomorokhov, Parameters of compton x-ray beams: Total yield and pulse duration, Phys. Rev. ST Accel. Beams 8 (2005) 030703. http://dx.doi.org/10.1103/PhysRevSTAB.8.030703. URL https://link.aps.org/doi/10.1103/PhysRevSTAB.8.030703.

[36] S. Chen, N.D. Powers, I. Ghebregziabher, C.M. Maharjan, C. Liu, G. Golovin, S. Banerjee, J. Zhang, N. Cunningham, A. Moorti, S. Clarke, S. Pozzi, D.P. Umstadter, MeV- Energy X rays from inverse compton scattering with laser-wakefield accelerated electrons, Phys. Rev. Lett. 110 (2013) 155003.

[37] E. Esarey, C.B. Schroeder, W.P. Leemans, Physics of laser-driven plasma-based electron accelerators, Rev. Modern Phys. 81 (2009) 1229–1285. http://dx.doi.org/10.1103/RevModPhys.81.1229. URL https://link.aps.org/doi/10.1103/RevModPhys.81.1229.

[38] K. Nakamura, W. Wan, N. Ybarrolaza, D. Syversrud, J. Wallig, W.P. Leemans, Broadband single-shot electron spectrometer for GeV-class laser-plasma-based accelerators, Rev. Sci. Instrum. 79 (5) (2008) 053301. http://dx.doi.org/10.1063/1.2929672.

[39] M. et al., ESTAR, PSTAR, and ASTAR: Computer programs for calculating stopping-power and range tables for electrons, protons, and helium ions (version 1.2.3). http://physics.nist.gov/Star. (Accessed 15 July 2014).

[40] M.J. Berger, J.H. Hubbell, S.M. Seltzer, J. Chang, J.S. Coursey, R. Sukumar, D.S. Zucker, K. Olsen, XCOM: Photon cross section database. http://www.nist.gov/pml/data/xcom/index.cfm. (Accessed 15 July 2014).

[41] S. Holland, An overview of CCD development at lawrence berkeley national laboratory, Exp. Astron. 14 (2) (2002) 83–89. http://dx.doi.org/10.1023/B:EXPA.0000004341.11906.bf. URL https://doi.org/10.1023/B:EXPA.0000004341.11906.bf.

[42] R. Turchetta, J. Berst, B. Casadei, G. Claus, C. Colledani, W. Dulinski, Y. Hu, D. Husson, J.L. Normand, J. Riester, G. Deptuch, U. Goerlach, S. Higueret, M. Winter, A monolithic active pixel sensor for charged particle tracking and imaging using standard VLSI CMOS technology, Nucl. Instrum. Methods Phys. Res. A 458 (3) (2001) 677–689. http://dx.doi.org/10.1016/S0168-9002(00)00893-7. URL http://www.sciencedirect.com/science/article/pii/S0168900200008937.

[43] J. Sempau, J. Fernndez-Varea, E. Acosta, F. Salvat, Experimental benchmarks of the monte carlo code penelope, Nucl. Instrum. Methods Phys. Res. B 207 (2) (2003)

107–123. http://dx.doi.org/10.1016/S0168-583X(03)00453-1. URL http://www.sciencedirect.com/science/article/pii/S0168583X03004531.

[44] B. Plimley, D. Chivers, A. Coffer, K. Vetter, Experimental benchmark of electron trajectory reconstruction algorithm for advanced compton imaging, IEEE Trans. Nucl. Sci. 60 (3) (2013) 2308–2313. http://dx.doi.org/10.1109/TNS.2013.2254498.

[45] B. Plimley, A. Coffer, Y. Zhang, K. Vetter, Angular sensitivity of modeled scientific silicon charge-coupled devices to initial electron direction, Nucl. Instrum. Methods Phys. Res. A 827 (2016) 18–23. http://dx.doi.org/10.1016/j.nima.2016.04.092. URL http://www.sciencedirect.com/science/article/pii/S0168900216303175.

[46] G. Knoll, Radiation Detection and Measurement, John Wiley & Sons, 2010.